Steel and Composite Structures, *Vol. 16, No. 5 (2014) 455-480*
DOI: http://dx.doi.org/10.12989/scs.2014.16.5.455

Compressive performances of concrete filled Square CFRP-Steel Tubes (S-CFRP-CFST)

Qingli Wang [*1] and Yongbo Shao [2a]

[1] *School of Civil Engineering, Shenyang Jianzhu University, Hunnandong Road 9, Shenyang, Liaoning, P.R. China*
[2] *School of Civil Engineering, Yantai University, Qingquan Road 32, Yantai, Shandong, P.R. China*

(*Received July 29, 2011, Revised October 29, 2013, Accepted December 23, 2013*)

Abstract. Sixteen concrete filled square CFRP-steel tubular (S-CFRP-CFST) stub columns under axial compression were experimentally investigated. The experimental results showed that the failure mode of the specimens is strength loss of the materials, and the confined concrete has good plasticity due to confinement of the CFRP-steel composite tube. The steel tube and CFRP can work concurrently. The load versus longitudinal strain curves of the specimens can be divided into 3 stages, i.e., elastic stage, elasto-plastic stage and softening stage. Analysis based on finite element method showed that the longitudinal stress of the steel tube keeps almost constant along axial direction, and the transverse stress at the corner of the concrete is the maximum. The confinement effect of the outer tube to the concrete is mainly focused on the corner. The confinements along the side of the cross-section and the height of the specimen are both non-uniform. The adhesive strength has little effect both on the load versus longitudinal strain curves and on the confinement force versus longitudinal strain curves. With the increasing of the initial stress in the steel tube, the load carrying capacity, the stiffness and the peak value of the average confinement force are all reduced. Equation for calculating the load carrying capacity of the composite stub columns is presented, and the estimated results agree well with the experimental results.

Keywords: square CFRP-steel composite tube; in-filled concrete; compressive performance; load carrying capacity; theoretical analysis

1. Introduction

Fiber Reinforced Plastic (FRP) is characterized by its high strength to weight ratio, high corrosion resistance, and ease of installation. Due to these advantages, it is used more and more in engineering practices. Fig. 1(a) shows a CFRP (Carbon Fiber Reinforced Plastic)-steel composite tank for contenting high pressure fuel gas used in motor vehicle. Its inner shell is made of steel and outer shell is made of CFRP, which utilizes rigidity and strength of the steel and tensile strength of the CFRP.

Fig. 1(b) shows CFRP-steel or GFRP (Glass Fiber Reinforced Plastic)-iron composite pipeline

*Corresponding author, Professor, E-mail: ceqlwang@sjzu.edu.cn
[a] Professor, E-mail: cybshao@ytu.edu.cn

http://www.techno-press.org/?journal=scs&subpage=8 ISSN: 1229-9367 (Print), 1598-6233 (Online)

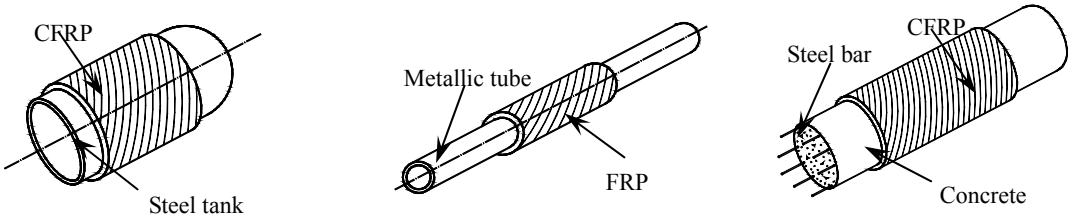

(a) Communications engineering (b) Municipal/chemical engineering (c) Civil engineering

Fig. 1 FRP used in engineering practices

system for transporting high pressure gas/liquid usually used in municipal/chemical engineering. Its inner tube is made of metal and outer tube is made of FRP, which also uses rigidity and strength of the metallic materials and tensile strength of the FRP composites. Additionally, wrapping FRP externally around the metallic tube is beneficial to corrosion resistance of the pipe. There are many these kinds of engineering in P.R. China.

Over the past several decades, FRP material has gained its popularity as a jacketing material in retrofitting/repairing existing (steel bar) Reinforced Concrete (RC) structures (as shown in Fig. 1(c)) (Fam and Rizkalla 2001, Teng *et al*. 2002, Wang and Restrepo 2001). Fig. 1(c) has another form: casting RC into a pre-fabricated CFRP tube to form a member (hereinafter referred to as CFRP-RC) for carrying load. Besides many experimental studies, there were also some corresponding theoretical analyses in the literatures (Jiang and Wu 2012, Yu *et al*. 2010a, b, Karabinis *et al*. 2008, Rousakis *et al*. 2008).

In recent years, Concrete Filled Steel Tubes (CFST) have become more widely accepted for these composite columns combining the advantages of both steel and concrete (Uy 2001, Han *et al*. 2001, Han 2007, Tao *et al*. 2009). They have proven to be economical as well, providing for rapid constructions and saving additional costs of formwork while also being labor saving. There were more applications about Circular CFST (C-CFST) because circular steel tube has better confinement effect on the concrete. However, Square CFST (S-CFST) also becomes popular in engineering practice for its advantage of simplifying construction of the joints. In-filled concrete can eliminate concave buckling but can't avoid convex buckling of the steel tube. The conditions will be encountered in practice that existing CFST are needed to add new functions or have slight damages. All of above are related to take some measures to reinforce/strengthen CFST. Therefore, casting concrete into a pre-fabricated CFRP-steel composite tube to form a member to carry load (Wang *et al*. 2005), or using CFRP to repair/strengthen existing CFST structures (Tao *et al*. 2007), both can form so-called Concrete Filled CFRP-Steel Tubular (hereinafter referred to as CFRP-CFST) structures.

Similar to CFST, CFRP-CFST can take advantages of the tri-axial compressed concrete sufficiently. Meanwhile, it can delay local buckling of the steel tube and has higher load carrying capacity and better durability. The combination of CFRP and the steel tube can remedy the defect of abrupt failure of the CFRP-RC structures as well.

Study on CFST structures is focused on C-CFST and S-CFST chiefly. Similarly, research on CFRP-CFST structures also concentrates in Circular CFRP-CFST (C-CFRP-CFST, as shown in Fig. 2(a)) and Square CFRP-CFST (S-CFRP-CFST, as shown in Fig. 2(b)). More recently, some research results have been reported on CFRP-CFST columns, which have preliminarily demonstrated

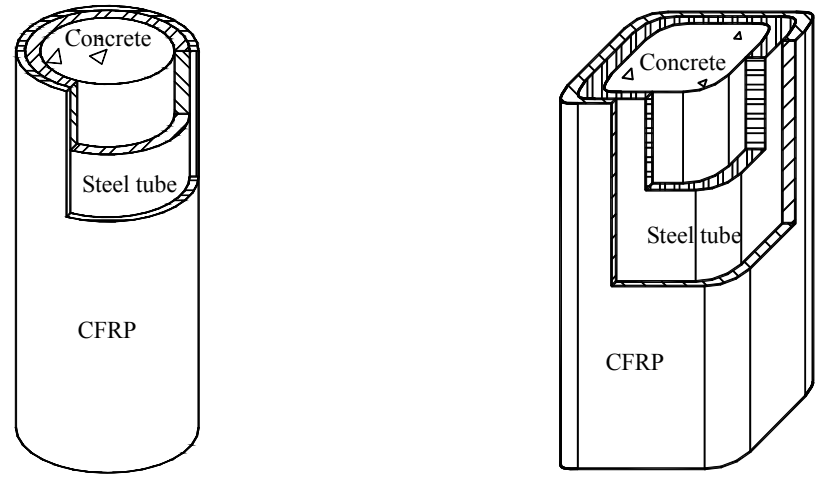

(a) C-CFRP-CFST (b) S-CFRP-CFST

Fig. 2 General view of CFRP-CFST

the effectiveness of CFRP wraps in increasing the axial load carrying capacity of CFST stub columns. Wang *et al*. (2005) initiated experimental study on C-CFRP-CFST stub columns. Tao *et al*. (2005, 2007) engaged in research of using CFRP to repair C-CFST or S-CFST structures after exposed to fire. Xiao *et al*. (2005) proposed a new C-CFST column system, where CFRP composites were used as additional confinement to the potential plastic hinge regions of the composite column. An analytical model was established for further research (Choi and Xiao 2010). Tests on behaviors of C-CFRP-CFST under compression and cyclic loads were conducted by Park *et al*. (2010). Most of these works use experimental measures to analyze the phenomenon, and the mechanism of CFRP-CFST is not studied deeply. Additionally, the determination and calculation of the load carrying capacity for this structure is still necessary to be studied in further work.

In order to discover the compressive performances of S-CFRP-CFST theoretically, in this paper, on the basis of experimental investigation, the load versus longitudinal strain curves, the failure modes of the specimens, cooperation between the steel tube and the CFRP and so on are discussed. The load versus longitudinal strain curves and the failure modes of S-CFRP-CFST stub columns under compressive load are simulated by using finite element software ABAQUS. Furthermore, the confinement effect provided by CFRP for the S-CFST stub columns is analyzed. Thereafter, the stress and strain distributions for materials and the transverse deformation are discussed respectively. Influences of adhesive strength and initial stress in the steel tube on the stub columns are investigated. Finally, index and parametric equations of the load carrying capacity for the S-CFRP-CFST stub columns are proposed.

2. Experimental investigation

2.1 General

Test on sixteen specimens, including twelve S-CFRP-CFST stub columns and four S-CFST

stub columns under compressive load, were conducted. Principal factors include characteristic compressive strength of the concrete (f_{ck}) and confinement factor of the CFRP (ξ_{cf}) (Wang *et al*. 2005) listed as follows

$$f_{ck} = 0.67 f_{cu} \tag{1}$$

$$\xi_{cf} = A_{cft} f_{cft} / (A_c f_{ck}) \tag{2}$$

where, f_{cu} is cubic compressive strength of the concrete, which is determined by six 150 mm cubes that are cast and cured in conditions similar to that of the related specimens; A_{cft} and f_{cft} are cross-sectional area and the ultimate tensile strength of the CFRP, respectively; A_c is cross-sectional area of the concrete, in which

$$f_{cft} = E_{cf} \varepsilon_{cftr} \tag{3}$$

where, E_{cf} is elasticity modules of the carbon fiber sheet; ε_{cftr} is the rupture strain of the CFRP, and its value is equal to 3000 $\mu\varepsilon$, and it is obtained by strain gauges attached on CFRP of the specimens.

Specimen details are provided in Table 1. In Table 1, specimens designations starting with SSC refer to Square Stub Columns, the next letter A, B, C and D distinguishing f_{ck} are of 22.3 MPa, 26.4 MPa, 32.8 MPa and 40.0 MPa, and the last cipher 0, 1, 2 or 3 refers to the number of layer(s) of the transverse CFRP (m). The length of the stub columns (L) was designed to be three times of the outer side-width of the steel tube (B_s), t_s is wall thickness of the steel tube, and ξ_s is confinement factor of the steel tube proposed by Han (2002)

$$\xi_s = A_s f_y / (A_c f_{ck}) \tag{4}$$

where, A_c and f_y are cross-sectional area and yield strength of the steel tube, respectively.

2.2 Material properties

Welded square steel tube was used, and radius of the inner chamfer is 5 mm (it should be pointed out that, due to the limitation of experimental instruments, the specimens have been designed in small-scale. The side-width of the cross-section is 140 mm, and this is why the corner radius is relatively smaller. Considering application in engineering, it is really necessary to carry out study on full-scale specimens in the future). Tensile tests on steel coupons cut from the original steel tubes were conducted. The measured properties of the steel tubes obtained from these tests are given in Table 2, where E_s, ε_{sy}, v_s, f_u and δ_s are elasticity modulus, yield strain, elasticity Poisson' ratio, the ultimate strength and elongation percentage of the steel tube, respectively.

All the specimens belong to a same series cast with one type of concrete. In all the concrete mixes, Portland cement (C), fly ash (FA), silica-based medium and coarse sand (S) were used as fine aggregate, limestone (G) with size of 5mm-15mm was adopted as course aggregate, and water (W) and MIGHTY 100 water reducing agent (SP) were used. The mix proportions of the concrete are summarized in Table 3.

Indices of the concretes are shown in Table 4, where E_c is elasticity modules of the concrete.

Table 1 Specimen labels and member capacities

No.	Specimens label	B_s (mm)	t_s (mm)	L (mm)	ξ_{cf}	m (layer (s))	f_{ck} (MPa)
1	SSC A-0	140	3.5	420	0	0	22.3
2	SSC A-1	140	3.5	420	0.11	1	22.3
3	SSC A-2	140	3.5	420	0.22	2	22.3
4	SSC A-3	140	3.5	420	0.33	3	22.3
5	SSC B-0	140	3.5	420	0	0	26.4
6	SSC B-1	140	3.5	420	0.09	1	26.4
7	SSC B-2	140	3.5	420	0.18	2	26.4
8	SSC B-3	140	3.5	420	0.28	3	26.4
9	SSC C-0	140	3.5	420	0	0	32.8
10	SSC C-1	140	3.5	420	0.07	1	32.8
11	SSC C-2	140	3.5	420	0.15	2	32.8
12	SSC C-3	140	3.5	420	0.22	3	32.8
13	SSC D-0	140	3.5	420	0	0	40.0
14	SSC D-1	140	3.5	420	0.06	1	40.0
15	SSC D-2	140	3.5	420	0.12	2	40.0
16	SSC D-3	140	3.5	420	0.18	3	40.0

No.	Specimens label	N_u^e (kN)	ε_{cftr}'	r (%)	ξ_s	$E_{cfsce}A_{cfsc}$ (10^3kN)	N_{max}^F (kN)
1	SSC A-0	919	-	0	1.45	902	1033
2	SSC A-1	969	3166	5.44	1.45	937	1107
3	SSC A-2	1094	3186	19.04	1.45	971	1129
4	SSC A-3	1107	2810	20.46	1.45	1006	1222
5	SSC B-0	1084	-	0	1.23	914	1187
6	SSC B-1	1107	3227	2.12	1.23	946	1200
7	SSC B-2	1201	2928	10.79	1.23	979	1237
8	SSC B-3	1266	3686	16.79	1.23	1011	1294
9	SSC C-0	1158	-	0	0.99	954	1180
10	SSC C-1	1187	3206	2.5	0.99	983	1204
11	SSC C-2	1297	3118	12	0.99	1013	1300
12	SSC C-3	1374	3023	18.65	0.99	1043	1400
13	SSC D-0	1470	-	0	0.81	1011	1549
14	SSC D-1	1582	3084	7.62	0.81	1039	1601
15	SSC D-2	1688	2902	14.83	0.81	1067	1742
16	SSC D-3	1799	2890	22.38	0.81	1095	1815

Table 2 Material properties of the steel tube

E_s (GPa)	f_y (MPa)	ε_{sy} (%)	v_s	f_u (MPa)	δ_s (%)
203	300	0.2878	0.28	425	24

Table 3 Mixture proportions of the concrete

Series	Strength grade of the cement	C	FA	S	G	W	SP
A	42.5	0.6	0.4	2.5	1.5	0.4	0.01
B	42.5	0.6	0.4	2	1.4	0.35	0.01
C	52.5	0.76	0.24	1.5	1.5	0.3	0.017
D	52.5	0.74	0.26	1.2	1.5	0.3	0.009

Table 4 Indices of the concrete

Series	A	B	C	D
f_{cu} (MPa)	33.0	39.4	49.0	59.7
E_c (GPa)	26.5	29.7	32.3	35.0

Table 5 Main technical properties of the carbon fiber sheets

Model number	f_{cf}' (GPa)	E_{cf} (GPa)	δ_{cf} (%)	w_{cf} (g/m^2)	t_{cf} (mm)
C200/200	4.57	226	2.02	200	0.111

Fig. 3 Typical failed CFRP coupon

The used carbon fiber sheet is made in EPO Company, Germany, which is a kind of high quality one-way sheet fabricated with TORAY T 700 12K that made in Japan. The tensile properties of the CFRP, determined from tensile tests of 6 flat coupons (as shown in Fig. 3), are given in Table 5, in which f_{cf}', δ_{cf} and w_{cf} are tension strength, elongation percentage and density of the carbon fiber sheet respectively, and t_{cf} is thickness of 1 layer sheet.

It should be pointed out that rupture strain value of the coupon tests as listed in Table 4 (δ_{cf} = 2.02%, 20200 $\mu\varepsilon$) is not the same as that of CFRP mounted on the specimens as given above (ε_{cftr} = 3000 $\mu\varepsilon$). This deviation is perhaps due to the different curvature of the CFRPs (Yu *et al*. 2006), and the real reason should be investigated in the future. ε_{cftr} was used later for Finite Element (FE) modeling and calculation of the load carrying capacity.

JGN-C, a kind of epoxy resin used for building structures that produced by Building Science Research Institute of Liaoning Province, P.R. China, was used for adhering the CFRP to the steel tube. Another epoxy resin, JGN-P, was adopted for gluing CFRPs together.

2.3 Specimen preparations

In preparing the S-CFRP-CFST specimens, carbon fiber sheets were applied using a hand lay-up method and were wrapped around the steel tube with the fiber direction perpendicular to axis of the steel tube. The finishing end of a sheet overlapped the starting end by 150 mm. The concrete was filled in layers. These specimens were then placed upright to air-dry until testing. Prior to testing, the top surfaces of the S-CFRP-CFST specimens were ground smoothly and flat. A steel plate with a thickness of 20 mm was then welded to the top of each specimen. Fig. 4 shows all S-CFRP-CFST stub columns before the test.

2.4 Test setup and instrumentation

A testing machine with capacity of 5000 kN was used for the compression tests on all specimens. Eight strain gauges, including four in the longitudinal direction and another four in the transverse direction, mounted on the steel tube surface of each specimen (Points 1, 2, 3 and 4 as shown in Fig. 5), were used to measure longitudinal strain of the steel tube (ε_{sl}) and transverse strain of the steel tube (ε_{st}) at the mid-height cross-section, respectively. In addition, four strain gauges in the transverse direction, mounted on the CFRP surface of each specimen (Points 1, 2, 3

Fig. 4 All specimens before test

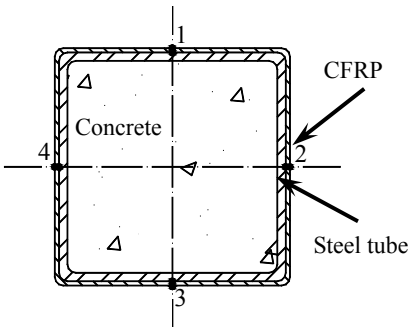

Fig. 5 Distribution of the strain gauges

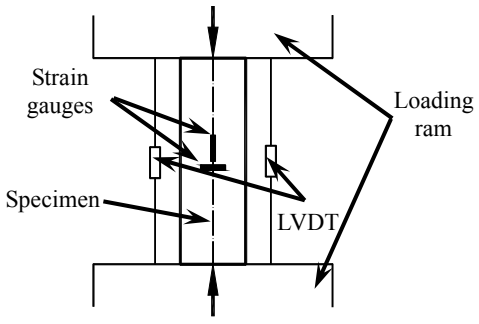

Fig. 6 Test arrangement

Fig. 7 In-site picture of the test

and 4 as shown in Fig. 5), were used to measure transverse strain of CFRP (ε_{cft}) at the mid-height cross-section.

Two Linear Variable Displacement Transducers (LVDTs) were used to measure axial shortening (Δ) of the specimens during the tests. IMP (Data acquisition system) was used for data logging. The test arrangement is shown in Fig. 6, and Fig. 7 is in-site picture of the test.

2.5 Test observations and failure modes

For the S-CFRP-CFST specimens, there is no obvious change in the appearance of the specimens during the initial loading process. Noise of the oxide layers peeling can be heard as axial load (N) increases. As load increases further, there appears local outward buckling near the mid-height cross-section and its nearby regions. When the load attains about 90% of the maximum load (N_{max}^{e}), the specimen deforms remarkably and some CFRPs fail gradually and the failure initiates at the corner of the specimens (At this state, the average value of the strains measured from 4 strain gauges glued at the center of the cross-section at the mid-height is named as rupture strain of the transverse CFRP for each specimen (ε_{cftr}'), and the values of ε_{cftr}' are tabulated in Table 1. The average value of the ε_{cftr}' is defined as the rupture strain of the transverse CFRP, (ε_{cftr})). Later on, their peak loads are attained and mid-height cross-section of the specimens convexes immediately accompanied by loud sound. The failure belongs to strength loss of the materials. Load carrying capacity drops rapidly after the maximum load. Specimens' failure continues as deformation increases, a large amount of CFRP begins to rupture and the fracture develops evenly from midst to both ends nearby. For the corresponding S-CFST specimens, appearances of local outward buckling of the steel tube are relatively earlier (about 70% of N_{max}^{e}) than those of the S-CFRP-CFST specimens, and the deformation velocity is higher than those of the S-CFRP-CFST specimens after the specimens reach elasto-plastic stage. All specimens after failure are shown in Fig. 8.

The CFRP of C-CFRP-CFST stub columns ruptures randomly along transverse direction (Che *et al*. 2012), while those of the S-CFRP-CFST stub columns occur mainly at the corners of the specimens. It is indicated that confinement of members provided by CFRP are not uniform for the S-CFRP-CFST stub columns. Additionally, rupture strain of the CFRP is about 3000 $\mu\varepsilon$, and this value is different from that of CFRP of the C-CFRP-CFST stub columns (5500 $\mu\varepsilon$) (Wang *et al*. 2005).

Fig. 9 shows failure modes of the concrete after cutting off the CFRP-steel composite tube. Fig. 9 indicates that concrete near the midst of columns was crushed. The convex deformations of concrete and the steel tube are identical. Compared to concrete without any confinement, both

(a) Series A (b) Series B (c) Series C (d) Series D

Fig. 8 All specimens after failure

(a) Specimen SSC B-0 (b) Specimen SSC B-3

Fig. 9 Failure modes of the in-filled concrete

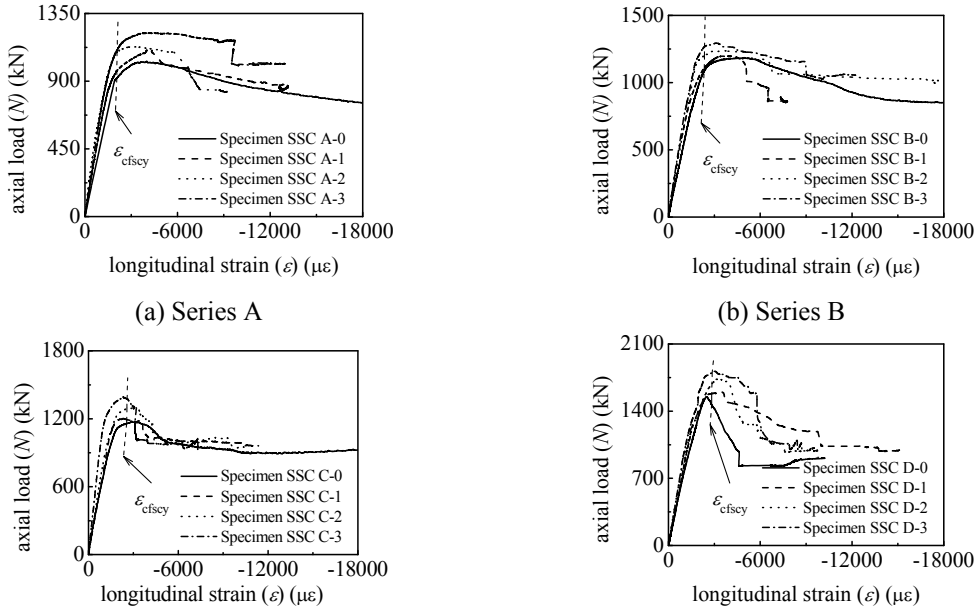

(a) Series A (b) Series B

(c) Series C (d) Series D

Fig. 10 N versus ε curves of the specimens

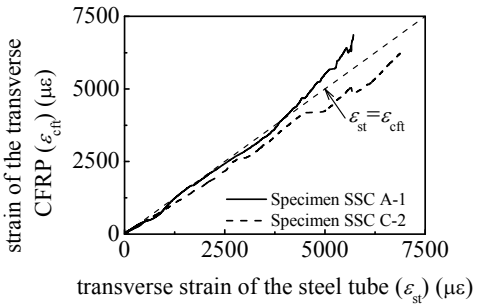

Fig. 11 ε_{cft} versus ε_{st} curves for several specimens

concrete confined with steel tube and concrete confined with CFRP-steel composite tube perform better plasticity.

2.6 Test results

2.6.1 Tested axial load versus longitudinal strain curves

The tested axial load versus longitudinal strain (ε) curves of the specimens are shown in Fig. 10. Fig. 10 indicates that the S-CFRP-CFST specimens are under elasticity in the initial stage because the curves are straight. The elasto-plastic stage of the specimens begins at the stage of about 80% of N_{max}^{e}, and the increasing rate of ε is faster than that of N. Softening stage of the curves begins after N exceeds N_{max}^{e}. During the softening process of the curves, N_{max}^{e} reduces quickly. The increase of ε is not remarkable in initial stage, and N reduces slowly and the increase of ε becomes remarkable in later stage. At this time, the plastic development of the steel tube tends to be rapid.

2.6.2 Cooperation of steel tube and CFRP

Fig. 11 illustrates ε_{cft} versus ε_{st} curves for several S-CFRP-CFST stub columns. It can be seen from Fig. 11 that from initial stage of loading till the CFRP rupturing, ε_{st} and ε_{cft} are the same approximately, and this means that the steel tube and the CFRP can work concurrently till failure. The same conclusion has been obtained from study on the C-CFRP-CFST stub columns conducted by Wang *et al*. (2005).

3. FE simulation

3.1 Stress versus strain relationship of materials

3.1.1 Steel

A 5-stages stress-strain relationship of steel used by Han (2007) is adopted here and Von Mises yielding criterion is used. The cold hardening effect at the corner of the steel tube is modeled by referring to research (Han 2007).

3.1.2 Concrete

For concrete confined by square CFRP-steel tube under compression, stress versus strain property is given based on experimental investigation as well as considering corresponding reported research about concrete confined by square steel tube under compression (Han 2007) as follow

$$y = \begin{cases} x(2-x) & (x \le 1) \\ \dfrac{x^{1+D}}{\beta(x-1)^{1.6+1.5/x}+x} & (1 < x \le \varepsilon_u/\varepsilon_0) \\ \dfrac{x}{\beta_s(x-1)^{1.6+1.5/x}+x} & (x > \varepsilon_u/\varepsilon_0) \end{cases} \tag{5}$$

$$y = \sigma_{cl}/\sigma_0 \tag{6}$$

$$x = \varepsilon_{\mathrm{cl}} / \varepsilon_0 \tag{7}$$

where σ_{cl} and σ_0 are longitudinal stress and the ultimate compressive stress of the concrete respectively, $\varepsilon_{\mathrm{cl}}$ and ε_0 are longitudinal strain and the ultimate compressive strain of the concrete respectively. D is a quantity related to confinement factor ratio (ξ') proposed by Wang *et al*. (2005); β is a quantity related to total confinement factor (ξ) proposed by Wang *et al*. (2005) before fracture of the transverse CFRP; β_{s} is a quantity related to ξ_{s} after fracture of the transverse CFRP; ε_{u} is longitudinal strain of the specimen (ε) corresponding to $N_{\max}^{\mathrm{e}}$, which is a function relating to ε_0 and ξ_{cf}

$$\sigma_0 = 1.12 f_{\mathrm{c}}' \tag{8}$$

$$\varepsilon_0 = \varepsilon_{\mathrm{c}} + (1382 - 159\xi)\xi^{0.2} \times 10^{-6} \tag{9}$$

$$\varepsilon_{\mathrm{c}} = (1300 + 12.5 f_{\mathrm{c}}') \times 10^{-6} \tag{10}$$

$$D = (1.545 - 1.238\xi')\xi' \tag{11}$$

$$\beta = f_{\mathrm{c}}'^{0.1} / (1.35\sqrt{1+\xi}) \tag{12}$$

$$\beta_{\mathrm{s}} = f_{\mathrm{c}}'^{0.1} / (1.2\sqrt{1+\xi_{\mathrm{s}}}) \tag{13}$$

$$\varepsilon_{\mathrm{u}} = \varepsilon_0 + (3535\xi_{\mathrm{cf}} + 58951\xi_{\mathrm{cf}}^{\,2}) \times 10^{-6} \tag{14}$$

$$\xi' = \xi_{\mathrm{cf}} / \xi_{\mathrm{s}} \tag{15}$$

$$\xi = \xi_{\mathrm{cf}} + \xi_{\mathrm{s}} \tag{16}$$

in above equations, f_{c}' is compressive strength of the cylinder concrete specimens, and its relationship with f_{cu} can be found in Ref. (Han 2007).

The softening property for concrete under tensile stress is simulated by energy criterion, as shown in Fig. 12. In Fig. 12, w is concrete crack width, w_1 is the maximum crack width, σ_t is tensile stress of the concrete, G_{f} is rupture energy of the concrete and σ_{t0} is the ultimate tension stress of the concrete.

$$G_{\mathrm{f}} = 40 + 4(f_{\mathrm{c}}' - 20) \quad (\mathrm{N/m}) \tag{17}$$

$$\sigma_{\mathrm{t0}} = 0.26(1.5 f_{\mathrm{ck}})^{2/3} \tag{18}$$

where f_{c}' is between 20 MPa-40 MPa and it is in MPa.

3.1.3 CFRP

The CFRP is assumed to be subjected to transverse tension only, and the stress value in other direction is assumed to be 0.001 MPa. Before fracture, the stress versus strain relationship is in accordance with Hooke's Law

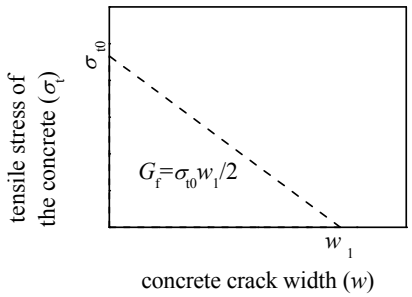

Fig. 12 Constitutive relationship of the tensile concrete

$$\sigma_{\text{cft}} = E_{\text{cf}}\varepsilon_{\text{cft}} \tag{19}$$

where σ_{cft} is stress of the transverse CFRP. The maximum σ_{cft} is f_{cft}.

3.2 FE model

3.2.1 Element type selection

The steel tube and the concrete are modeled with 3-D brick elements C3D8R with reduced integration. Membrane element M3D4 with four nodes is used for modeling the CFRP, and this membrane element has only in-plane stiffness but no bending stiffness.

3.2.2 Mesh discretization

The convergent analysis is carried out by using refined mesh in FE analysis. An original relative coarse mesh is used to conduct FE analysis, and then the mesh is doubled to carry out FE analysis again to assess the convergence of the numerical results. If the FE results with original and refined meshes converge, i.e., the relative error is less than 1%, the original mesh is suitable for numerical analysis. Otherwise, the mesh will be refined again to conduct additional analysis till the convergence of the FE results is satisfied. Considering the corner effect, the mesh around the corner is refined. Fig. 13 is view of the FE mesh.

(a) Cross-section element (b) Longitudinal element of the steel tube

Fig. 13 Mesh discritization

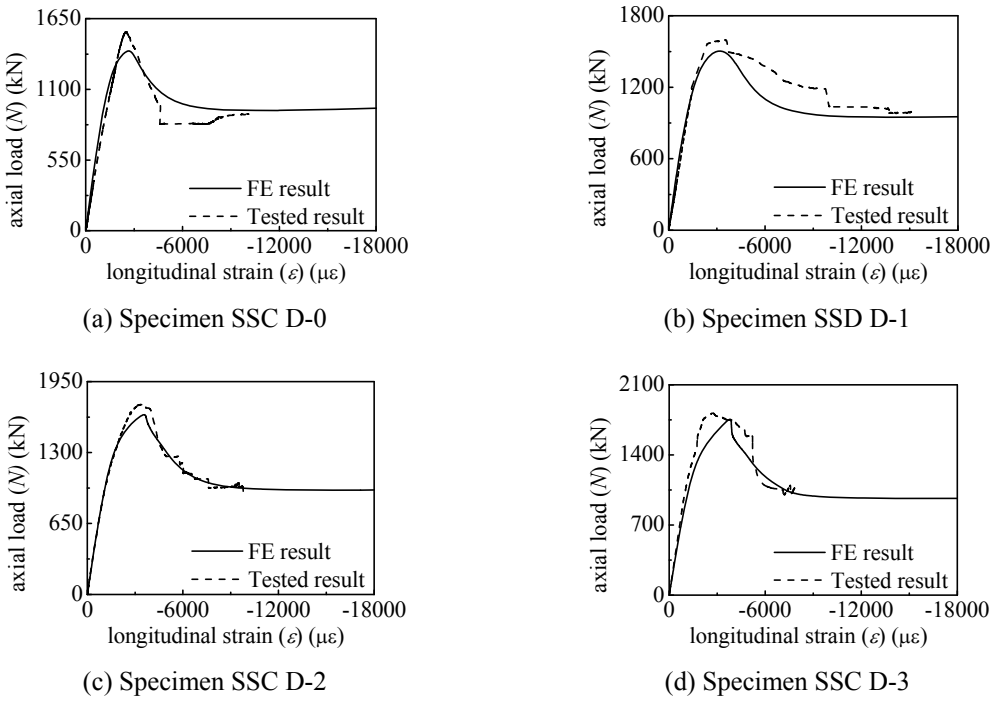

Fig. 14 Comparisons between FE results and tested results of N versus ε curves for several specimens

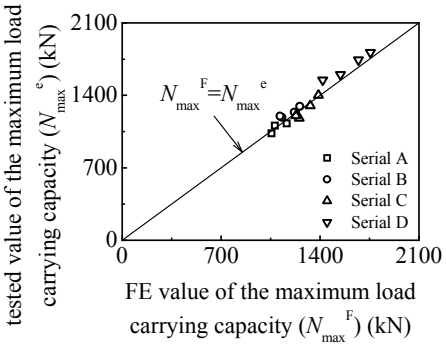

Fig. 15 Comparisons between N_{max}^{F} and N_{max}^{e}

3.2.3 Interface model

Hard contact is used for contact interface between the steel tube and concrete, i.e., the pressure perpendicular to the contact surfaces (p) can be transferred completely between the two surfaces. The tangential force between the steel tube and the concrete surfaces is simulated by using Columb model, i.e., shear force can be transferred between surfaces. According to the test results, the CFRP is bound to the steel tube, and it is assumed that no slip exists between the CFRP and the steel tube. Same nodal freedoms are used for the contact elements between the CFRP and the steel

tube. When CFRP reaches its ultimate strength and is fractured, CFRP loses its confinement to the steel tube. In the tangential direction of the contact surfaces between the end plate and the concrete, there is no slipping, and hard contact assumption is used in normal direction of contact surfaces.

3.2.4 Boundary conditions

Only the axial freedom at the loading point is released, and all the freedoms at the other end are fixed. The displacement is applied along the axis direction of the columns. To avoid the deformation of the end plate and to model the boundary condition more accurately, the stiffness of the end plate is set to be very large. The elastic modulus and Poisson's ratio are 10^{12} MPa and 0.0001, respectively.

3.3 FE results

3.3.1 FE results of axial load versus longitudinal strain curves

To verify the reliability of the above presented FE method, 16 stub columns are analyzed by using ABAQUS software. The FE results together with the tested results for several stub columns are plotted in Fig. 14.

FE value of the maximum load carrying capacity (N_{max}^{F}) for all specimens are listed in Table 1 and plotted against N_{max}^{e} in Fig. 15. It can be found from Figs. 14 and 15 that the FE results agree reasonably well with the experimental results.

3.3.2 Deformed modes

Figs. 16 and 17 are deformed modes of the S-CFRP-CFST stub columns and the S-CFST stub columns, respectively, where the red arrows are principal stress vectors of the CFRP. At this state, the global axial strain of the S-CFRP-CFST columns is about 48000 $\mu\varepsilon$ and that of the S-CFST columns is about 52000 $\mu\varepsilon$. It can be seen that deformed mode of the S-CFRP-CFST displays a convex at the mid-height cross-section, while deformed mode of the S-CFST displays several convexes around the midst of the column.

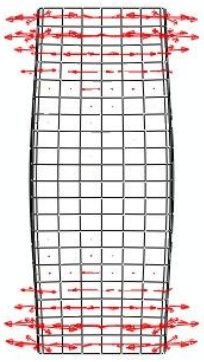

(a) FE result

(b) Test result

Fig. 16 Deformed modes of the S-CFRP-CFST stub column

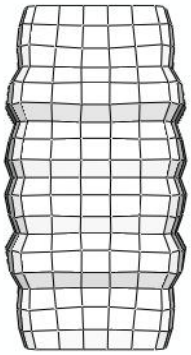

(a) FE result

(b) Test result

Fig. 17 Deformed modes of the S-CFST stub column

4. Theoretical analysis

Compressive performances of the S-CFRP-CFST stub columns are discussed deeply by using a typical model, the details of the typical model are listed as follows: L = 420 mm, B_s = 140 mm, t_s = 3.5 mm, f_y = 300 MPa, f_{ck} = 40 MPa, ξ_{cf} = 0.17, ξ_s = 0.99, $E_c = 4700\sqrt{f_c'}$ (MPa) and Poisson's ratio of the concrete (v_c) is of 0.2.

4.1 Stress versus longitudinal strain curves

Fig. 18 shows σ (stress) versus ε curves of the S-CFRP-CFST stub columns, in which σ_{cfsc} and σ_{sl} are nominal compression stress of the specimens and longitudinal stress of the steel tube, respectively, $\sigma_{cfsc} = N / A_{cfsc}$, in which A_{cfsc} is cross-sectional area of the S-CFRP-CFST specimens. For the purpose of a clear expression, σ_{sl} is divided by 5 and σ_{cft} is divided by 10, also, p is multiplied by 10. It can be seen from Fig. 18 that the steel yields before N reaches N_{max}^e for the specimens. However, the stresses in the concrete do not reach the ultimate value. At this time, σ_{cft} increases in an approximate linear relationship, and such increase rate becomes bigger and bigger. When the stresses in the concrete reach the ultimate value, the specimens are also under their ultimate state (the peak stress point in the figure). At this stage, only few CFRP are fractured at the corner of the steel tube. The value of σ_{cft} is still increasing, and such increasing rate is dropping slowly. In the dropping stage of the σ_{cl} versus ε curves, the σ_{cfsc} versus ε curves also begin to drop. After the plastic stage of the curves initiates, σ_{sl} begins to decrease. After the hardening point of steel material, σ_{sl} has an increasing tendency. At this stage, CFRP begins to be fractured in a large amount with the increasing compression deformation of the specimens. The stresses in the CFRP reduce to zero rapidly and the strains increase quickly.

For S-CFST stub columns, the value of p is negative in initial stage (Han 2007), and the calculated results in Fig. 18 show that the value of p is still negative in initial stage even the stub columns are wrapped by CFRP to form S-CFRP-CFST stub columns. This may be due to the fact that the Poisson's ratio of the steel tube is larger than that of in-filled concrete. Thus the interfaces between the steel tube and the concrete have a separate tendency. The above stage is relatively short, and it ends when the strain reaches about 1500 $\mu\varepsilon$. With the increase of the axial load, the transverse deformation ratio (Poisson's ratio) of the concrete is also increasing continuously, and

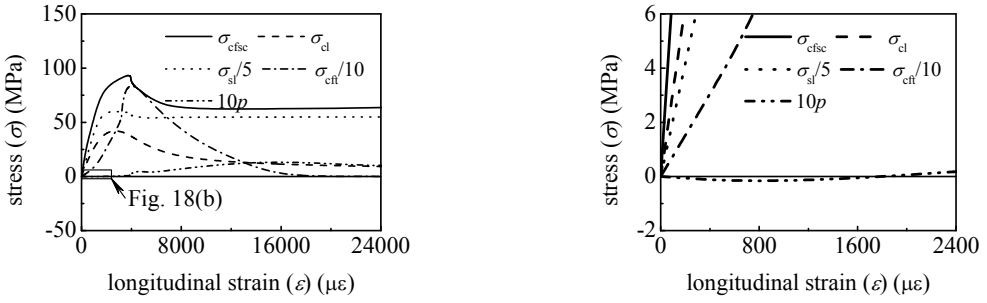

(a) Full view (b) Magnified part

Fig. 18 σ versus ε curves of the S-CFRP-CFST stub columns

finally it exceeds the Poisson's ratio value of the steel tube. At this time, interaction between steel tube and concrete appears, and the average longitudinal stress of the concrete is about 85% of the ultimate stress. Simultaneously, the steel tube begins to yield. With the increase of the longitudinal stress, the confinement also increases continuously. The confinement weakens gradually after the steel tube yields.

For C-CFST stub column, the value of p is negative in initial stage (Han 2007, Che *et al*. 2012). After wrapping CFRP to form C-CFRP-CFST stub columns, the confinement force is always positive during the whole loading process (Che *et al*. 2012). This means the confinement efficiency of CFRP to C-CFST stub columns is much better than that of CFRP to S-CFST stub columns.

4.2 Stress analysis

4.2.1 Stress in steel tube

Variations of σ_{sl} and transverse stress of the steel tube (σ_{st}) at mid-side on the mid-height cross-section of the S-CFRP-CFST stub columns under compression are plotted together in Fig 19, where σ_s is stress of the steel tube. It is noted that Fig. 19 only provides the stress magnitude and ignores the stress sign. As seen from Fig. 19, the value of σ_{sl} increases rapidly while the value of σ_{st} increases very slowly in initial loading process. As the loading increases, interaction between the steel tube and concrete occurs, and σ_{st} begins to increase. Furthermore, the value of σ_{sl} begins to decrease after its peak value and σ_{st} keeps a gradual increase.

Variations of σ_{sl} and σ_{st} at mid-side along height of the S-CFRP-CFST stub columns under axial compression are shown in Fig. 20, where $\sigma_{sl,L/4}$, $\sigma_{sl,3L/8}$ and $\sigma_{sl,L/2}$ are longitudinal stresses of the steel tube at $L/4$, $3L/8$ and $L/2$ from the end plate of the specimen respectively, $\sigma_{st,L/4}$, $\sigma_{st,3L/8}$ and $\sigma_{st,L/2}$ are transverse stresses of the steel tube at $L/4$, $3L/8$ and $L/2$ from the end plate of the specimen respectively. Fig. 20 shows that σ_{st} increases with the increase of the distance to the specimen end plate, and this conclusion is coincident with that of the C-CFRP-CFST stub columns (Che *et al*. 2012). However, the distribution of σ_{sl} is basically uniform along the height of the specimen, which is different from the conclusion of C-CFRP-CFST stub columns (Che *et al*. 2012).

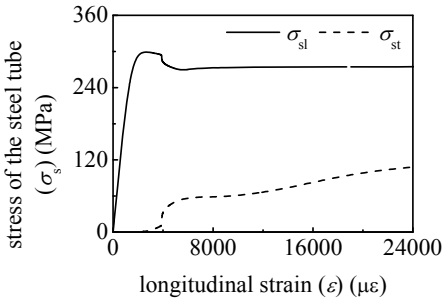

Fig. 19 σ_s versus ε curves at mid-side on mid-height cross-section of the S-CFRP-CFST stub columns

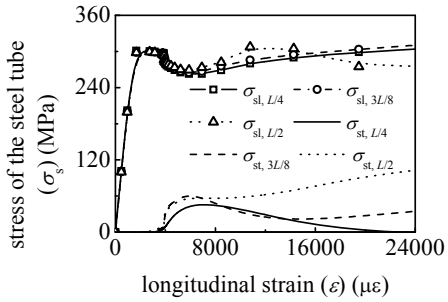

Fig. 20 σ_s versus ε curves at mid-side along height of the S-CFRP-CFST stub columns

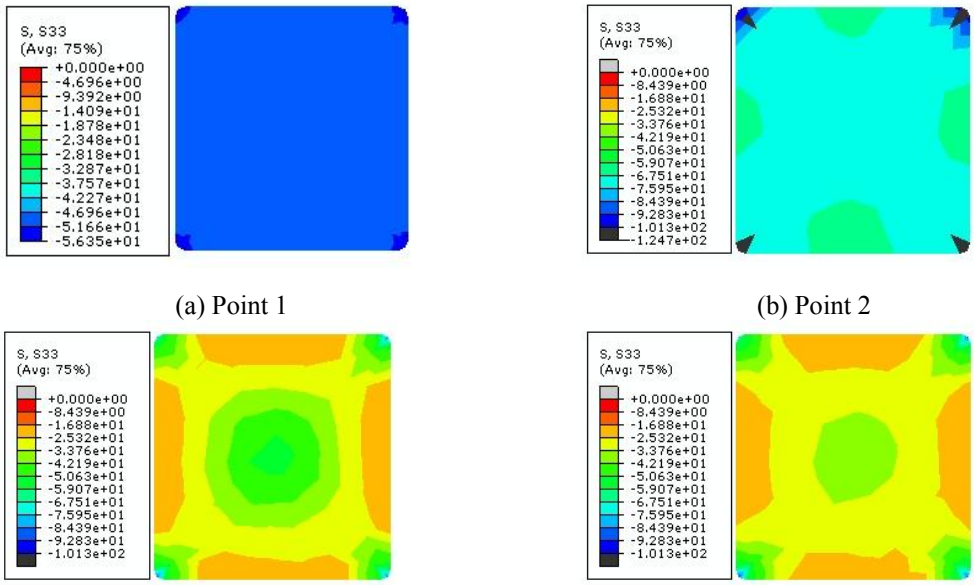

(a) Point 1 (b) Point 2

(c) Point 3 (d) Point 4

Fig. 21 Distribution of σ_{cl} on the mid-height cross-section of the S-CFRP-CFST stub columns

4.2.2 Stress in concrete on mid-height cross-section

Distribution of σ_{cl} on the mid-height cross-section of the S-CFRP-CFST stub columns is shown in Fig. 21, in which point 1 is yield point of the steel tube, and the specimen reaches its maximum load carrying capacity at point 2. Strain at point 3 is two times of the strain corresponding to the maximum load carrying capacity, and the strain at point 4 is 20000 $\mu\varepsilon$. From Fig. 21, it is found that the stresses at point 1 are basically uniform with the value of about f_c'. Only in a small range at the corner, the compressive stress has a value about $1.1f_c'$. At point 2, the stress value of the concrete is about $1.4f_c'$, and the peak stress is located at the corner with a value of about $2f_c'$. At point 3, the longitudinal stresses in the center and at the corner begin to decrease, and the value of the stress at the corner is about $1.7f_c'$. The stresses in the concrete center at point 4 are almost consistent. Overall, the longitudinal stresses of the concrete distribute along the section non-uniformly. The stress at the corner is the maximum, and the stress in the centroid is the minimum. For C-CFRP-CFST stub columns, the longitudinal stresses of the concrete distribute always uniformly in the circumferential direction (Che *et al*. 2012).

To understand this in a clear way, the longitudinal stresses of the concrete at different positions (d) of the above critical points on the Section 1-1 and Section 2-2 (as shown in Fig. 23) of S-CFRP-CFST stub columns are plotted in Fig. 22. It can be seen from Fig. 22 that the stresses of the concrete on Sections 1-1 and 2-2 distribute generally uniformly when the steel tube yields. After the specimens reach the ultimate load carrying capacity, the stresses of the concrete on Section 1-1 have peak value at the corner. As the longer distance from the corner, such stresses decrease rapidly. Meanwhile, they vary little along the plain region along the steel tube. For the Section 2-2, the stresses at the corner also reach the peak value. Such stresses decrease rapidly

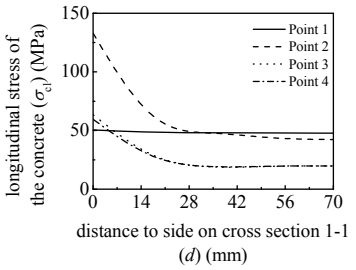

(a) Cross-section 1-1

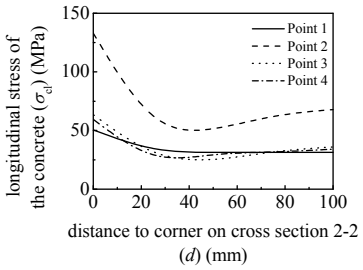

(b) Cross-section 2-2

Fig. 22 σ_{cl} at center point in different elements of the S-CFRP-CFST stub columns

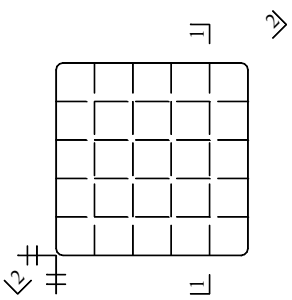

Fig. 23 view of the cross-sections 1-1 and 2-2

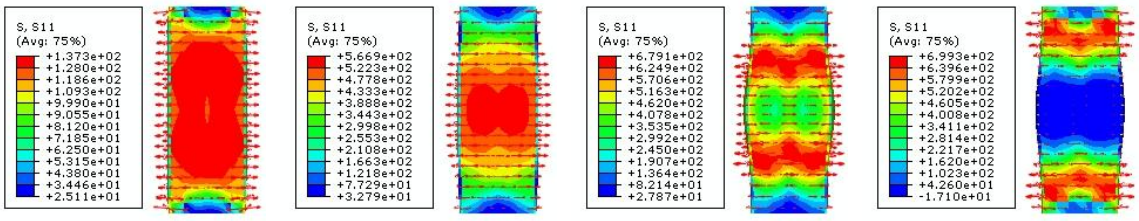

(a) Point 1 (b) Point 2 (c) Point 3 (d) Point 4

Fig. 24 Stress distribution of transverse CFRP of the S-CFRP-CFST stub columns

with the distance to the corner becomes bigger, too. When it approaches to the center of in-filled concrete, the stress value is increasing accordingly. However, such value is still smaller than that at the corner.

4.2.3 Stress in CFRP

Fig. 24 shows stress of the transverse CFRP for the S-CFRP-CFST stub columns. From Fig. 24, it can be found that the stresses of the transverse CFRP distribute uniformly in the initial loading stage (Point 1). With the increase of load, the stresses on the mid-section increase remarkably (Point 2). The deformation of specimens is still uniform along the direction of height. After the failure stage (Point 3), the stresses on the cross-section at mid-height decrease gradually. With the continuous failure of CFRP, the cross-section at mid-height appears apparent plastic deformation. At this time, the stresses are mostly concentrated at the 1/4 of the height. Finally, the stresses on the cross-section at mid-height become zero (Point 4), and such process agrees well with the observation of the experiment. It is also coincident with the corresponding conclusions of C-CFRP-CFST stub columns (Che *et al*. 2012).

4.3 Transverse deformation

Fig. 25 shows the variation of transverse deformation (Δ′) on cross-section at mid-height of the

S-CFRP-CFST stub columns during the loading process, where – $0.8N_{max}^{e}$ and $-0.6N_{max}^{e}$ denote the loading decreases to 0.8 and 0.6 of N_{max}^{e}, respectively. As Fig. 25 shows, the deformations at the corner and at the mid-side of the steel tube have little difference during the initial loading process. As load increases, the transverse deformation at the mid-side increases fast accordingly, even exceeds the one at the corner. It means that the confinement of concrete applied by the steel tube is focused on the corner of the steel tube, and this conclusion is coincident with experimental observation.

Fig. 26 shows the variation of transverse deformation on cross-section at mid-height of the S-CFST stub columns during the loading process. From the comparison between Figs. 25 and 26, the transverse deformation of S-CFRP-CFST is obviously smaller than that of S-CFST during the whole loading process from initial stage to the ultimate load carrying capacity stage. After the ultimate load carrying capacity, the transverse deformation of S-CFRP-CFST exceeds that of S-CFST as the fracture of CFRP. From the comparison of the final transverse deformation, it is found that the increasing magnitude of the transverse deformation of S-CFRP-CFST is bigger than that of S-CFST. This tells that CFRP can improve the stiffness of the specimen effectively before its fracture, and delay the deformation of the specimen.

Fig. 27 shows distribution of transverse strain of the steel tube for the S-CFRP-CFST stub columns and the S-CFST stub columns. It can be seen that the transverse deformation of S-CFRP-CFST is remarkably smaller than that of S-CFST, and this shows CFRP provides

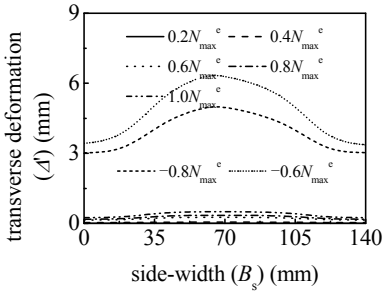

Fig. 25 Transverse deformation on mid-height cross-section of the S-CFRP-CFST stub columns

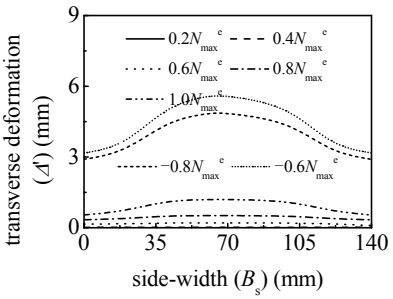

Fig. 26 Transverse deformation on mid-height cross-section of the S-CFST stub columns

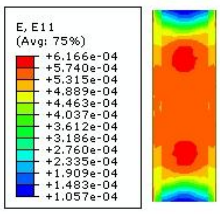

(a) Point 1 of the S-CFRP-CFST

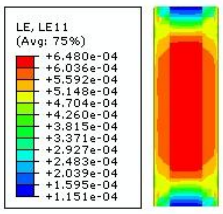

(b) Point 1 of the S-CFST

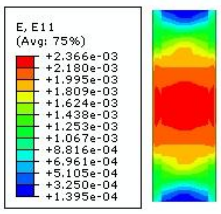

(c) Point 2 of the S-CFRP-CFST

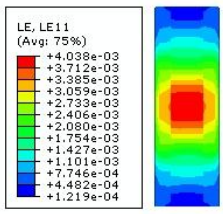

(d) Point 2 of the S-CFST

Fig. 27 Distribution of transverse strain of the steel tube

effective confinement to the CFST. This conclusion is coincident with that of C-CFST stub columns (Che *et al*. 2012).

4.4 Confinement force

4.4.1 Confinement force along side

Fig. 28 is variation of p at same height for the S-CFRP-CFST stub columns during loading process. It can be seen from Fig. 28 that the confinement is maximum at the corner of the steel tube, and it decreases rapidly as the distance to the corner of the steel tube increases. At the corner of the steel tube, the confinement decreases relatively fast after it reaches the peak value. With the expansion of concrete volume, the confinement presents increasing tendency again, but only with a little magnitude.

4.4.2 Confinement force along height

Fig. 29 is variation of p at different heights for the S-CFRP-CFST stub columns during the loading process. Due to the non-uniformity of the confinement force along the boundary of the cross-section, the averaged confinement at the height is adopted. It can be seen from Fig. 29 that the confinement force at the section of the mid-height is maximum while the confinement at both ends of the specimen is relatively smaller. The confinement at the $L/4$ height is already much closer to the confinement at the mid-height. When it is much closer to the mid-height, the increased magnitude is not remarkable although the stress still increases.

4.4.3 Average confinement force

From the above analysis, it can be concluded that the confinement of the steel tube to the concrete is not uniform along the width and the height of the specimen. To investigate the overall variation of the confinement, the averaged confinement is used for the study. Fig. 30 shows the curves between the averaged confinement at the mid-height against ε with different ξ_{cf} and different strength grades of the concrete. Fig. 30 makes a clear statement that the increase of ξ_{cf} and the strength of concrete can improve the confinement force of specimens.

To make a clear understanding on the action of the CFRP in S-CFRP-CFST, Δp is defined as the difference of the averaged confinements force between the S-CFRP-CFST stub columns and

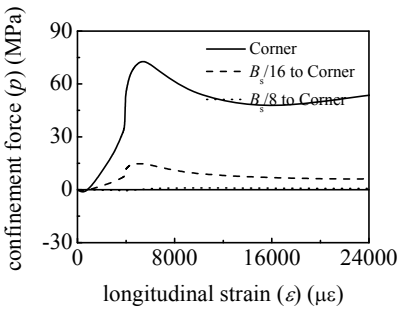

Fig. 28 p versus ε curves at same height of the S-CFRP-CFST stub columns

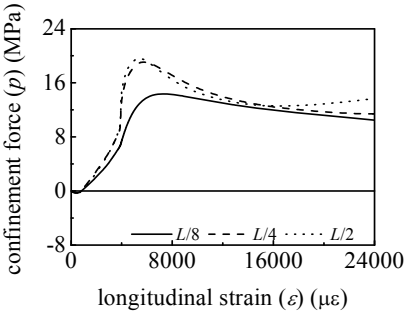

Fig. 29 p versus ε curves at different height of the S-CFRP-CFST stub columns

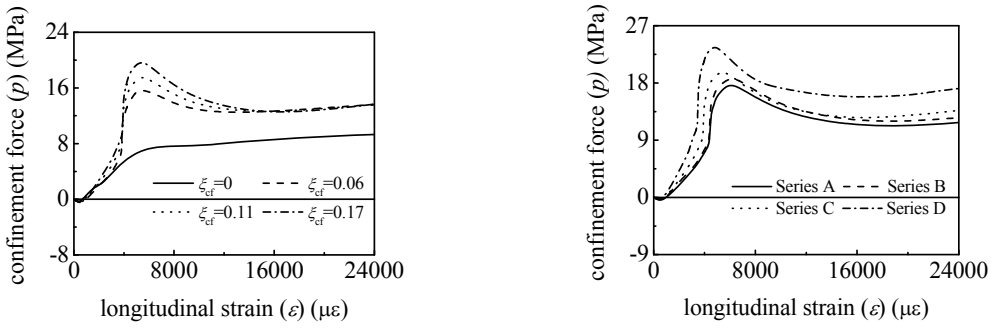

(a) Influence of confinement factor of the CFRP (b) Influence of strength of the concrete

Fig. 30 Confinement force versus strain curves of the S-CFRP-CFST stub columns

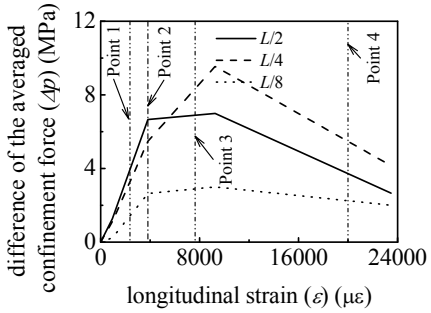

Fig. 31 Δp versus ε curves

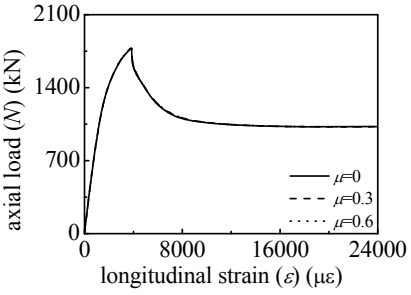

Fig. 32 Influence of adhesive strength on N versus ε curves of the S-CFRP-CFST stub columns

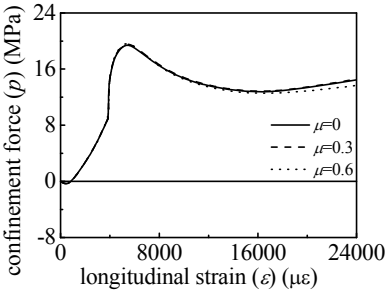

Fig. 33 Influence of adhesive strength on p versus ε curves of the S-CFRP-CFST stub columns

the corresponding S-CFST stub columns. The Δp versus ε curves are plotted by using the results at the typical points to describe the tendency of the averaged confinement. The confinement efficiency is then assessed from the slope of the curves (as shown in Fig. 31). From the results in Fig. 31, it can be found that the slope of the curve at the $L/2$ of the height is bigger than those at the $L/4$ and $L/8$ of the height before the ultimate strain of the specimen. It shows that the bigger

confinement efficiency is located at the mid-height. With the increase of the deformation, the slope of the curve at the $L/2$ of the height is apparently smaller than those at the $L/4$ and $L/8$ of the height. This means CFRP at the mid-height already fails, and thus the main confinement has been transferred to the $L/4$ of the height. Such above conclusions agree well with experimental observation.

4.5 Effect of adhesive strength and initial stress in steel tube on columns

4.5.1 Adhesive strength

Three friction factors (μ) with values of 0 (no adhesive strength), 0.3 and 0.6 are used to model the different adhesive strength between the steel tube and the concrete. Figs. 32 and 33 show the influence of adhesive strength on N versus ε curves and on p versus ε curves of the S-CFRP-CFST stub columns, respectively. Figs. 32 and 33 show that the adhesive strength has almost no effect on the two curves. This conclusion is coincident with that of the C-CFRP-CFST stub columns (Che *et al*. 2012).

4.5.2 Initial stress in steel tube

The distribution of the initial compressive stresses σ_{s0} on the cross-section of the steel tube is assumed to be uniform in the finite element model. Fig. 34 shows load versus strain curves of the S-CFRP-CFST stub columns under axial compression with different initial stress coefficients (β_0), and

$$\beta_0 = \sigma_{s0} / \phi_s f_y \tag{20}$$

where σ_{s0} is initial stress in the steel tube, and ϕ_s is stability coefficient of the square hollow steel tube.

The initial stress of the steel tube reduces the elastic stage of S-CFRP-CFST stub columns, which can be seen from Fig. 34. With the increase of the initial stress, the load carrying capacity decreases gradually, and the corresponding ultimate strain and the initial strain increase in a little magnitude, i.e., the initial stress reduces the stiffness of the specimen slightly. Such conclusion is also coincident with that of the C-CFRP-CFST stub columns (Che *et al*. 2012).

A series of p versus ε curves for S-CFRP-CFST stub columns under axial compression with different initial stress coefficients are plotted in Fig. 35. From Fig. 35, it is found that the initial

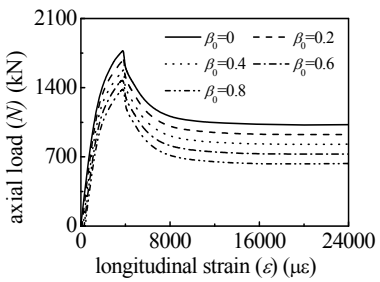

Fig. 34 Influence of σ_{s0} on N versus ε curves of the S-CFRP-CFST stub columns

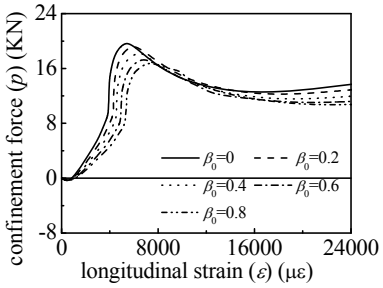

Fig. 35 Influence of σ_{s0} on p versus ε curves of the S-CFRP-CFST stub columns

stress makes initial compressive strains yield in the steel tube before they work together, and this delays the interaction between the steel tube and concrete. With the increase of the coefficient of the initial stress, the average peak value of the confinement decreases as well. This conclusion is similar with that of the C-CFRP-CFST stub columns (Che *et al*. 2012).

5. Load carrying capacity index and stiffness

5.1 Definition of load carrying capacity index

Expressions for load carrying capacity index for C-CFRP-CFST stub column were proposed by Che *et al*. (2012). However, for S-CFRP-CFST stub column, it seems to be necessary to provide new equations because the fracture of CFRP and the maximum load occur simultaneously for C-CFRP-CFST stub column while CFRP is fractured before the load reaches its maximum value for S-CFRP-CFST stub column.

The stress versus longitudinal strain relationship of the S-CFRP-CFST stub column is investigated based on the FE analysis of many models to define load carrying capacity index of the S-CFRP-CFST stub columns (f_{cfscy}) reasonably. The validity range of these models is: f_y = 200 – 500 MPa, f_u = 30 – 120 MPa, steel ratio $\alpha_s = A_s / A_c$ = 0.03 – 0.2, ξ_{cf} = 0 – 0.55, $E_c = 4700\sqrt{f_c'}$ (MPa) and ν_c = 0.2. Finally, the load carrying capacity at the longitudinal strain ε_{cfscy} which is determined from the stress versus longitudinal strain curves (as shown in Fig. 10) is defined as f_{cfscy}. ε_{cfscy} is expressed as follow

$$\varepsilon_{cfscy} = 1300 + 12.5 f_c' + 18 f_c' \xi^{0.2} \quad (\mu\varepsilon) \tag{21}$$

ε_{cfscy} is defined on the following facts: firstly, the elastic stage of the σ_{cfscy} versus ε_{sl} curve is basically completed at the strain value about ε_{cfscy}. Secondly, the steel tube and the concrete both reach the ultimate state at ε_{cfscy}, but CFRP is not fractured. Finally, the stress of the σ_{cfscy} versus ε_{sl} curve increases very fast before ε_{cfscy}, while the strain increases relatively slowly. However, after ε_{cfscy}, the stress increases slowly while the strain increases faster.

5.2 Parametric equation of load carrying capacity

The relationship between γ_c = (= f_{cfscy} / f_{ck}) and ξ can be expressed with simple equation as shown in Fig. 36. The equation is obtained from regression analysis and f_{cfscy} is listed as follow

$$f_{cfscy} = (1.18 + 0.85\xi) f_{ck} \tag{22}$$

The load carrying capacity (N_u) of the S-CFRP-CFST stub column under axial compression can be calculated by using the following equation

$$N_u = A_{cfsc} f_{cfscy} \tag{23}$$

5.3 Validation of expression

Fig. 37 shows the comparison of the estimated results of N_u (N_u^c) and the experimental results

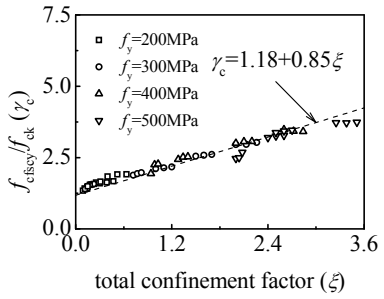

Fig. 36 γ_c versus ξ relationship

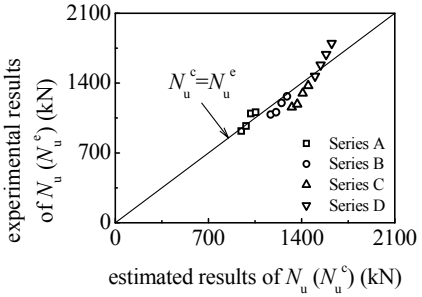

Fig. 37 Comparisons between N_u^c and N_u^e for the specimens

of N_u (N_u^e) for the S-CFRP-CFST stub column. It is found that the simplified equation can produce reasonably accurate estimations. The average of N_u^c / N_u^e is 1.013 and the mean square deviation is 0.071. The calculated results by the equation are safe in general. In case of no CFRP (S-CFST), Eqs. (21)-(23) are reduced to the corresponding calculating equations of the S-CFST stub columns given by Han (2002).

5.4 Load carrying capacity increment ratio

For specimens with the same f_{ck}, named N_u^e of S-CFST as N_{u0}^e, and that of S-CFRP-CFST as N_{um}^e, then r is load carrying capacity increment ratio

$$r = \left(N_{um}^{\ e} - N_{uo}^{\ e}\right) \Big/ N_{uo}^{\ e} \times 100\% \tag{24}$$

The values of r are listed in Table 1 and plotted versus m in Fig. 38. Fig. 38 shows that, comparing with the S-CFST stub columns, N_{um}^e are all enhanced, and r increases nearly linearly with the increment of m.

5.5 Stiffness

It could be found from computation that the following equation can be used to calculate the longitudinal stiffness ($E_{cfsce}A_{cfsc}$) of the S-CFRP-CFST stub columns

$$E_{cfsce} = f_{cfscp} \big/ \varepsilon_{cfscp} \tag{25}$$

$$f_{cfscp} = \left[0.263\left(f_y/235\right) + 0.365\left(30/f_{cu}\right) + 0.104\right] f_{cfscy} \tag{26}$$

$$\varepsilon_{cfscp} = 3.01\times10^{-6} f_y \tag{27}$$

where f_{cfscp} is nominal proportional limit of the S-CFRP-CFST stub columns, and ε_{cfscp} is the corresponding strain at the nominal proportional limit.

Eqs. (25)-(27) are also suitable for S-CFST stub columns (ξ_{cf} = 0). The $E_{cfsce}A_{cfsc}$ of the tested

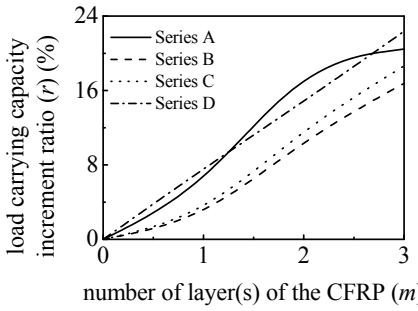

Fig. 38 Influence of *m* on load carrying capacity increment ratio (*r*)

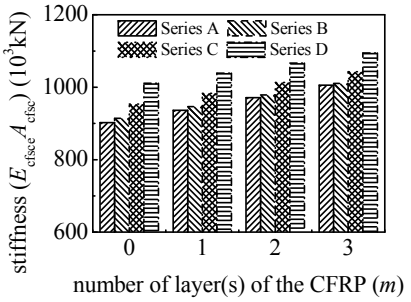

Fig. 39 Stiffness comparison for specimens

specimens are tabulated in Table 1 and shown in Fig. 39. As can be seen that the stiffness of the specimen is enhanced with the increase of CFRP layers and the strength of concrete.

6. Conclusions

The following conclusions can be drawn based on this study:

- Failure mode of the S-CFRP-CFST stub columns is strength loss of materials. CFRP postpones outward buckling of the steel tube and concrete has excellent plastic in-filled behavior. The steel tube and the CFRP work concurrently before failure.
- Load versus longitudinal strain curves of the S-CFRP-CFST stub columns are analyzed using ABAQUS, and it is found that the numerical results agree well with experimental results although they are generally safe. The load versus longitudinal strain curves can be classified into elastic stage, elasto-plastic stage and softening stage.
- Outer tube provides no confinement force for concrete during initial loading process, and the confinement force is concentrated on corners. Increasing of both the confinement factor and strength of the concrete can enhance the average confinement force.
- The initial stress in the steel tube postpones the mutual reaction between the steel tube and the concrete, while it has a little influence on the peak value of the confinement force; adhesive strength has little effect on load versus longitudinal strain curves and on confinement force versus longitudinal strain curves of the S-CFRP-CFST stub columns.
- In the validity range of the parameters presented in this study, the proposed parametric expression can be used to calculate load carrying capacity of the S-CFRP-CFST stub columns reasonably. Load carrying capacity and longitudinal stiffness of the S-CFRP-CFST stub columns increase with the increase of CFRP layers.

Acknowledgments

The research reported in the paper is part of the Project 51378320 supported by Natural Science Foundation of China (NSFC) and the Project 2013003004 supported by Public Welfare Foundation of Liaoning Province, P.R. China. Their financial supports are highly appreciated.

References

Che, Y., Wang, Q.L. and Shao, Y.B. (2012), "Compressive performances of the concrete filled circular CFRP-steel tube (C-CFRP-CFST)", *Int. J. Adv. Steel Construct.*, **8**(4), 311-338.

Choi, K.K. and Xiao, Y. (2010), "Analytical model of circular CFRP confined concrete-filled steel tubular columns under axial compression", *J. Compos. Construct.*, **14**(1), 125-133.

Fam, A.Z. and Rizkalla, S.H. (2001), "Confinement model for axially loaded concrete confined by circular FRP tubes", *ACI Struct. J.*, **98** (4), 451-461.

Han, L.H. (2002), "Tests on stub columns of concrete-filled RHS sections", *J. Construct. Steel Res.*, **58**(3), 353-372.

Han, L.H. (2007), *Concrete Filled Steel Tubular Structures-Theory and Practice*, China Science Press, Beijing, P.R. China. [In Chinese]

Han, L.H., Zhao, X.L. and Tao, Z. (2001), "Tests and mechanics model of concrete-filled SHS stub columns, columns and beam-columns", *Steel Compos. Struct., Int. J.*, **1**(1), 51-74.

Jiang, J.F. and Wu, Y.F. (2012), "Identification of material parameters for Drucker-Prager plasticity model for FRP confined circular concrete columns", *Int. J. Solid. Struct.*, **49**(3-4), 445-456.

Karabinis, A.I., Rousakis, T.C. and Manolitsi, G.E. (2008), "3D finite element analysis of substandard columns strengthened by fiber reinforced polymer sheets", *ASCE J. Compos. Construct.*, **12**(5), 531-540.

Park, J.W., Hong, Y.K. and Choi, S.M. (2010), "Behaviors of concrete filled square steel tubes confined by carbon fiber sheets (CFS) under compression and cyclic loads", *Steel Compos. Struct., Int. J.*, **10**(2), 187-205.

Rousakis, T.C., Karabinis, A.I., Kiousis, P.D. and Tepfers, R. (2008), "Analytical modelling of plastic behaviour of uniformly FRP confined concrete members", *J. Compos. Part B: Eng.*, **39**(7-8), 1104-1113.

Tao, Z., Han, L.H. and Zhuang, J.P. (2005), "Using CFRP to strengthen concrete-filled steel tubular columns: stub column tests", *Proceeding of the 4th International Conference on Advances in Steel Structures*, Shanghai, P.R. China, June.

Tao, Z., Han, L.H. and Zhuang, J.P. (2007), "Axial loading behavior of CFRP strengthened concrete-filled steel tubular stub columns", *Adv. Struct. Eng.*, **10**(1), 37-46.

Tao, Z., Uy, B., Han, L.H. and Wang, Z.B. (2009), "Analysis and design of concrete-filled stiffened thin-walled steel tubular columns under axial compression", *Thin-Wall. Struct.*, **47**(12), 1544-1556.

Teng, J.G., Chen, J.F., Smith, S.T. and Lam, L. (2002), *FRP-Strengthened RC Structures*, John Wiley & Sons, Ltd., Hoboken, NJ, USA.

Uy, B. (2001), "Strength of short concrete filled high strength steel box columns", *J. Construct. Steel Res.*, **57**(2), 113-134.

Wang, Q.L., Gu, W. and Zhao, Y.H. (2005), "Experimental study on concentrically compressed concrete filled circular CFRP-steel composite tubular stub columns", *China Civil Eng. J.*, **38**(10), 44-48. [In Chinese]

Wang, Y.C. and Restrepo, J.I. (2001), "Investigation of concentrically loaded reinforced columns confined with Glass Fiber-Reinforced Polymer Jackets", *ACI Struct. J.*, **98**(3), 377-385.

Xiao, Y., He, W.H. and Choi, K.K. (2005), "Confined concrete-filled tubular columns", *ASCE J. Struct. Eng.*, **131**(3), 488-497.

Yu, T., Teng, J.G., Wong, Y.L. and Dong, S.L. (2010a), "Finite element modeling of confined concrete-I: Drucker-Prager type plasticity model", *Eng. Struct.*, **32**(3), 665-679.

Yu, T., Teng, J.G., Wong, Y.L. and Dong, S.L. (2010b), "Finite element modeling of confined concrete-II: Plastic-damage model", *Eng. Struct.*, **32**(3), 680-691.

Yu, T., Wong, Y.L., Teng, J.G., Dong, S.L. and Lam, E.S. (2006), "Flexural behavior of hybrid FRP-concrete-steel double-skin tubular members", *J. Compos. Construct.*, **10**(5), 443-452.

CC